Conformations of the rhodopsin third cytoplasmic loop grafted onto bacteriorhodopsin

J Bernard Heymann[1], Matthias Pfeiffer[2], Volker Hildebrandt[2], H Ronald Kaback[3], Dimitrios Fotiadis[1], Bert de Groot[4], Andreas Engel[1], Dieter Oesterhelt[2] and Daniel J Müller[1,5]*

Background: The third cytoplasmic loop of rhodopsin (Rho EF) is important in signal transduction from the retinal in rhodopsin to its G protein, transducin. This loop also interacts with rhodopsin kinase, which phosphorylates light-activated rhodopsin, and arrestin, which displaces transducin from light-activated phosphorylated rhodopsin.

Results: We replaced eight residues of the EF loop of bacteriorhodopsin (BR) with 24 residues from the third cytoplasmic loop of bovine Rho EF. The surfaces of purple membrane containing the mutant BR (called IIIN) were imaged by atomic force microscopy (AFM) under physiological conditions to a resolution of 0.5–0.7 nm. The crystallinity and extracellular surface of IIIN were not perturbed, and the cytoplasmic surface of IIIN increased in height compared with BR, consistent with the larger loop. Ten residues of Rho EF were excised by V8 protease, revealing helices E and F in the AFM topographs. Rho EF was modeled onto the BR structure, and the envelope derived from the AFM data of IIIN was used to select probable models.

Conclusions: A likely conformation of Rho EF involves some extension of helices E and F, with the tip of the loop lying over helix C and projecting towards the C terminus. This is consistent with mutagenesis data showing the TTQ transducin-binding motif close to loop CD, and cysteine cross-linking data indicating the C-terminal part of Rho EF to be close to the CD loop.

Addresses: [1]M.E. Müller-Institute for Structural Biology, Biozentrum, University of Basel, Klingelbergstrasse 70, CH-4056 Basel, Switzerland, [2]Max-Plank-Institut für Biochemie, Membranbiochemie, Am Klopferspitz 18, D-82152 Martinsried, Germany, [3]Howard Hughes Medical Institute, Departments of Physiology and Microbiology & Molecular Genetics, Molecular Biology Institute, University of California Los Angeles, 90095-1662 Los Angeles, CA, USA, [4]Max-Plank-Institut für Biophysikalische Chemie, Arbeitsgruppe für theoretische molekulare Biophysik, Am Faßberg 11, D-37077 Göttingen, Germany and [5]Max-Plank-Institut für molekulare Zellbiologie und Genetik, Pfotenhauerstrasse 108, D-01307 Dresden, Germany.

*Corresponding author.
E-mail: Daniel.Mueller@unibas.ch

Key words: AFM, G-protein-coupled receptor, *Halobacterium salinarum*, molecular modeling, purple membrane

Received: **10 February 2000**
Revisions requested: **23 March 2000**
Revisions received: **31 March 2000**
Accepted: **18 April 2000**

Published: **31 May 2000**

Structure 2000, **8**:643–653

0969-2126/00/$ – see front matter

Introduction

Membrane proteins with seven transmembrane α helices constitute a large group of proteins including ion pumps in archaebacteria and G-protein-coupled receptors in eukaryotes. The availability of the structure of the closely related seven-helix archaebacterial photo-activated proton pump, bacteriorhodopsin (BR), allows us to explore questions about the structure of other seven transmembrane helix proteins, in particular rhodopsin (Rho) [1,2]. In addition to the helical fold, both BR and Rho have a retinal as a photo-active chromophore, which undergoes conformational changes on the absorption of light. The photoisomerization causes some α helices of BR to shift [3,4] and the polypeptide loop connecting helices E and F (EF loop) moves on the protein surface [5–9]. In Rho, the absorption of a photon by the retinal causes the second (CD) and third (EF) loops on the cytoplasmic surface to interact with its G protein, transducin [10–12]. The activated rhodopsin is phosphorylated on the C-terminal loop by rhodopsin kinase [13], which also binds to loops CD and EF [14]. Subsequently, arrestin binds to the first (AB) and EF loops [15]. The EF loop is therefore important in binding to three proteins involved in the rhodopsin photocycle.

Some evidence has been gathered that the EF loop might be structured and extend far above the membrane surface [16,17]. On the basis of spin-labeling studies, a simple model was proposed in which the Rho EF loop within Rho itself is mainly formed by the extension of helices E and F above the membrane to end in a short turn around residues Gln238 and Glu239 [16]. Nuclear magnetic resonance (NMR) studies and circular dichroism (CD) studies of the isolated loop in solution indicate

little change in conformation compared with a complex comprising all four cytoplasmic surface loops [17]. In contrast to the spin-labeling study, however, the NMR model of the Rho EF loop peptide in solution is consistent with the extension of helix E, but not of helix F, suggesting the turn to be around Thr243 [17]. It is therefore probable that the Rho EF loop introduced in BR would also adopt a particular conformation, with potential extension of helices E and F.

Here we were interested in answering several questions. If we replace the native BR EF loop with the third loop from bovine Rho, does it adopt a particular conformation within the BR framework? What is the most likely conformation? Is such a conformation relevant to its function within rhodopsin? This is only a first step in studying the cytoplasmic surface loops of rhodopsin, as well as our understanding of what is required to transfer such loops to other frameworks.

One tool that is able to determine features on surfaces such as extended loops on native proteins, is atomic force microscopy (AFM) [18,19], recently illustrated by comparison with X-ray diffraction and electron crystallography data [20]. Using the structural similarity between Rho and BR, we replaced eight residues from the BR EF loop with 24 residues from the Rho EF loop to create the mutant, IIIN. Next, we used AFM to image purple membranes with this construct and compared it with wild-type BR to determine the loop orientation. Numerous loops were modeled onto the BR frame to determine probable conformations consistent with the AFM data. The data and modeling indicated that, on the BR frame, the loop lies over the C terminus and does not extend as far from the membrane as current Rho models suggest.

Results

Replacing the BR EF loop with the Rho cytoplasmic loop III

The most prominent loop on the cytoplasmic surface of BR, the EF loop (Figure 1a) [20], was replaced by the corresponding loop of Rho (Figure 1b), shown to be involved in binding to transducin [12]. Eight residues from BR were replaced with 24 residues from Rho to produce the mutant, IIIN, confirmed by the ~2 kDa increased molecular mass as determined using sodium dodecylsulphate polyacrylamide gel electrophoresis (SDS–PAGE) (Figure 1c). The parent BR construct used has a point mutation, Asp96→Asn, that has a slightly blue-shifted absorption spectrum with a somewhat lower extinction coefficient (peak at 564 nm compared with wild-type BR at 568 nm). The Asp96→Asn mutant also shows some altered kinetics of the photocycle, however, these can be compensated for by adding azide (unpublished observations). The insertion of the Rho loop into this Asp96→Asn mutant did not change its spectroscopic properties and photochemical activity (unpublished observations).

Figure 1

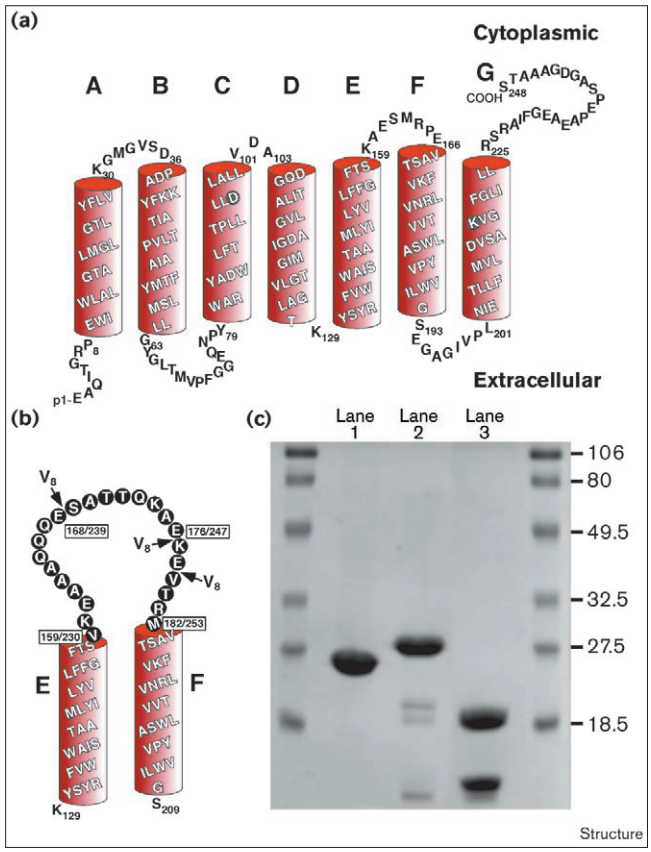

Replacement of the Rho third cytoplasmic loop onto BR. **(a)** Topological model of wild type BR. **(b)** Eight residues in loop EF of BR were replaced with 24 residues from loop III of bovin Rho to produce the mutant IIIN (indicated by the filled circles, the numbering in the boxes give the residue in IIIN first and the residue in the Rho loop second). V8 protease cleaves this loop after the glutamate residues indicated by the arrows. **(c)** V8 protease digestion of IIIN. Lane 1, wild-type BR; lane 2, mutant IIIN; lane 3, mutant IIIN digested with V8 protease in 25 mM Tris-HCl pH 7.9.

The mutant IIIN was digested with V8 protease, cutting on the C-terminal side of accessible glutamate residues, producing two bands at 18.5 and 8.5 kDa (Figure 1c). BR itself was not degraded by V8 protease, which indicates that Glu161 (which occurs in both BR and IIIN) is not accessible to the enzyme under these conditions. Interestingly, BR solubilized in SDS was cleaved [21], showing that under the disruptive effects of this detergent a part of the EF loop becomes accessible to V8 protease. Consistent with the SDS–PAGE result, electrospray ionization mass spectro-metry of the IIIN mutant after digestion with V8 protease gives two major peaks at 18425 and 8573 Da, compared with the 28499 Da for the intact protein. The digestion fragments that are best in agreement with these molecular masses are 14–168 (18442 Da) and 179–271 (8560 Da). It is concluded that a part of the Rho EF loop (SATTQKAEKE; in single-letter amino acid

code) and a small C-terminal fragment (seven residues) are excised by V8 protease.

AFM imaging shows an intact crystal for IIIN

Wild-type and IIIN purple membranes (PMs) were imaged in buffer at low resolution to assess the quality and heights of the sheets, and at high resolution to locate surface structures. The low-resolution imaging showed similar diameters (0.5 μm–1 μm) for the wild-type and IIIN PM sheets. The membranes adsorbed onto the mica surface without folding or cracking, satisfying the requirements for high resolution imaging [19]. The average height of the PM sheets measured in absence of electrostatic repulsion was found to be 5.6 ± 0.4 nm for BR [22] and 6.0 ± 0.4 nm for IIIN.

The extracellular and cytoplasmic faces of the PM were identified in previous AFM studies by specific antibody labeling [23]. The topographs show well-ordered trigonal two-dimensional (2D) crystals, with unit-cell parameters of $a = b = 6.2 \pm 0.2$ nm, and $\gamma = 120^\circ$ for both BR and IIIN. The root mean square (rms) deviation from threefold symmetry ranged from 9 to 12%, indicating strong preservation of the trigonal lattice. Crystal defects of individual proteins were used to determine the maximum height difference between protein and lipid membrane (i.e., the dynamic range), again the same for both BR and IIIN on the extracellular surfaces, 0.6 ± 0.1 nm (Table 1).

Because the extracellular loops of IIIN should be the same as for BR, the extracellular surface provides a good test for any unforeseen effects of the replacement of loop EF. The AFM topographs revealed almost identical extracellular surface features for both wild-type BR and IIIN (Figures 2a–e). The most prominent protrusion, the BC loop, is evident in the center of each monomer (Figures 2b,d), and the standard deviation maps differ very little between the two cases (Figures 2c,e). The formation and nature of the PM crystal are thus not affected by the mutation.

The cytoplasmic surface of IIIN shows a large change

High-resolution AFM imaging of the cytoplasmic surface of the IIIN PM at low force (50–100 pN) proved to be more difficult than with the wild-type PM. Submolecular resolution of the IIIN surface was only observed at a low salt concentration (50 mM KCl). Therefore, an electrostatic cushion [24] is required to avoid excessive deformation of the sample by the tip, suggesting that the surface structure is highly flexible. This is reflected in the higher standard deviation recorded for IIIN compared with wild-type PM (Table 1).

Low force imaging of the wild-type cytoplasmic PM shows one prominent peak in each BR monomer corresponding to the location of the EF loop (Figure 2i). Similarly, each monomer in the IIIN PM has one prominent protrusion, slightly shifted and projecting towards the C terminus at the end of helix G (Figures 2f,g). The height of the cytoplasmic surface increased from 0.8 nm in the wild-type PM to 1.5 nm in the IIIN PM, representing a significant increase in volume, consistent with the net addition of 16 residues. The standard deviation map of the IIIN PM indicates two variable regions (Figure 2h), one between helices E and F, which is also present in BR (Figure 2j), and one lying over helix C which is completely absent in the wild-type map. These features suggest that the Rho loop follows a course from helix E, over helix C, towards helix G, and back to helix F.

Imaging of both PMs at slightly enhanced force (increased force of 50–100 pN) resulted in the EF loops being pushed away, allowing underlying structures to be imaged (Figures 2k,l,n) [25]. The conformational change induced by higher force is fully reversible, which suggests that the Rho EF loop is a rather flexible element on the cytoplasmic surface of the BR molecule. What emerges are the AB and CD loops, and the C terminus, which are comparable in location and appearance to the loops of wild-type BR (Figure 2n). The IIIN standard deviation

Table 1

Measured variables of purple membrane AFM topographs.

Surface	Height range* (nm)	Standard deviation range (nm)	Resolution†(nm)		Force (pN)	KCl (mM)
			FRC	SNNR		
WT PM ext	0.6	0.07–0.12	0.5	0.7	100	100
IIIN PM ext	0.6	0.09–0.18	0.5	0.7	100	150
WT PM cyt	0.8	0.07–0.19	0.6	0.8	100	100
IIIN PM cyt	1.5	0.32–0.43	0.7	1.0	50–100	50
WT PM cyt (HF)‡	0.6	0.07–0.12	0.4	0.6	150	100
IIIN PM cyt (HF)‡	0.6	0.16–0.34	0.4	0.6	100–150	50
IIIN PM cyt (Dig)§	0.7	0.10–0.17	0.6	0.8	100	100

*The height range essentially gives the height above the lipid bilayer surface. †FRC, Fourier ring correlation; SSNR, spectral signal-to-noise ratio. ‡HF, high force imaging (> 100 pN). §Dig, digested with V8 protease.

Figure 2

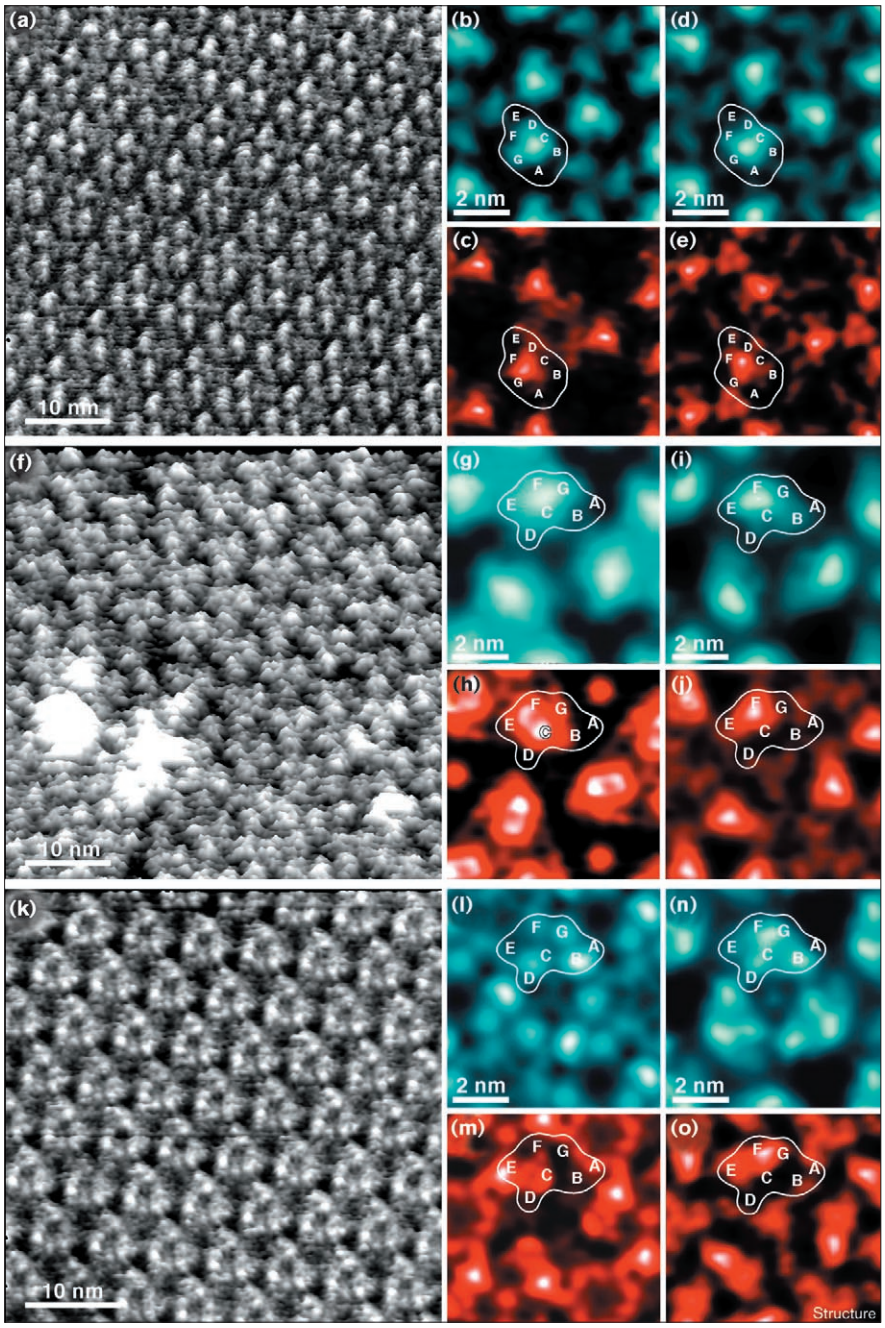

Extracellular and cytoplasmic surfaces of wild type and mutant IIIN PMs imaged by AFM. **(a)** Topograph of the native IIIN extracellular surface. **(b)** Threefold symmetrized correlation average of (a). **(c)** Standard deviation map of (b). **(d)** Threefold symmetrized average and **(e)** standard deviation map of an AFM topograph of the extracellular wild-type PM surface. **(f)** AFM topograph of the native IIIN cytoplasmic surface at low force (<100 pN). **(g)** Threefold symmetrized correlation average of (f). **(h)** Standard deviation map of (g). **(i)** Correlation average of the cytoplasmic surface of wild-type BR at low force (<100 pN). **(j)** Standard deviation map of (i). **(k)** AFM topograph of the native IIIN cytoplasmic surface at high force (>100 pN). **(l)** Threefold symmetrized correlation average of (k). **(m)** Standard deviation map of (l). **(n)** Correlation average of the cytoplasmic surface of wild-type BR at high force (>100 pN). **(o)** Standard deviation map of (n). The gray levels in the maps correspond to the height and standard deviation ranges shown in Table 1. The outlined BR shape and the position of the α-helical ends facing the extracellular and cytoplasmic surfaces (named A–G) were derived from atomic models. The unit-cell parameters are $a = b = 6.2$ nm and $\gamma = 120°$.

map also shows a significantly higher variability compared with the wild-type (Figure 2m,o and Table 1), mostly associated with helix E. In no instance are the last ~20 residues of the C terminus observed, and it is considered to be completely unstructured for both BR and IIIN. It is concluded that the only major difference in the cytoplasmic surface of the IIIN PM compared with wild-type is the long Rho EF loop, and that BR forms a good, stable framework for this loop.

Digestion of the Rho EF loop

Digestion of the IIIN PM with V8 protease (Figure 1b) did not affect the crystallinity (Figure 3a). Low-force AFM imaging shows a significant reduction in the major protrusion (Figure 3b) compared with the undigested surface (Figure 2i). The ends of helices E and F are now clearly visible, with most flexibility assigned to helix F in the standard deviation map (Figure 3c). Mass spectrometry indicated that a ten-residue fragment of loop Rho EF

and seven residues of the C terminus are removed (see above). The cut at Glu249 (Rho numbering) leaves a few residues extending from helix F. The cut at Glu239 (Rho numbering) leaves a long segment (approximately eight residues) neither seen in the AFM surface, nor in the standard deviation map. This suggests that the end of helix E is highly disordered. This is similar to the C terminus, where helix G ends at Phe230 (BR numbering) underneath the AFM surface, leaving the last 17 residues too flexible to be imaged.

Modeling the Rho EF loop

Interpretation of the AFM topographs with regard to atomic coordinate data requires a conversion from the 2D image format to a 3D format consistent with the 3D BR model. The AFM data of the two surfaces of each PM were converted to a 3D envelope, using the AFM height measurements to fix the separation of the surfaces (see the Materials and methods section). The BR model fits perfectly between the surfaces without further manipulation, providing confidence in the orientation and alignment. In particular, the EF loop of BR fits into the major protrusion on the cytoplasmic surface as seen by AFM (Figure 4a).

Eight residues of the EF loop of the BR model of Belrhali *et al.* [26] were replaced by 24 residues of the third loop of Rho using the program WHAT IF [27]. In all further manipulations and molecular dynamics, the BR framework of the new model was kept unmodified or restrained strongly. This is consistent with the AFM data, showing that the BR EF loop for the wild-type PM, and the Rho EF loop of the IIIN PM, are the major flexible structures on the cytoplasmic surfaces. The other loops exhibit lower B factors, lower variability between the different atomic models of BR, and increased stability during AFM imaging [20].

Many different conformations of the Rho EF loop were generated manually in WHAT IF [27] and O [28]. To produce a significant basis for assessing different loop conformations, these models were subjected to many rounds of sampling conformational flexibility using the package Concoord [29]. Concoord examines likely conformational changes using distance restraints derived from the model. Here we started from a model built by hand, then generated ten models with Concoord. We picked the one differing the most from the original, and used this for a subsequent round of model generation. Alternatively, we picked the one in best agreement with the AFM data as measured by occupancy (see the Materials and methods section). With several starting models and using up to a hundred rounds of model generation, we produced over a thousand models, covering a large part of the conformational space allowed for the loop on the rigid BR framework. These models were subject to a principle component analysis to extract the major axes of collective

Figure 3

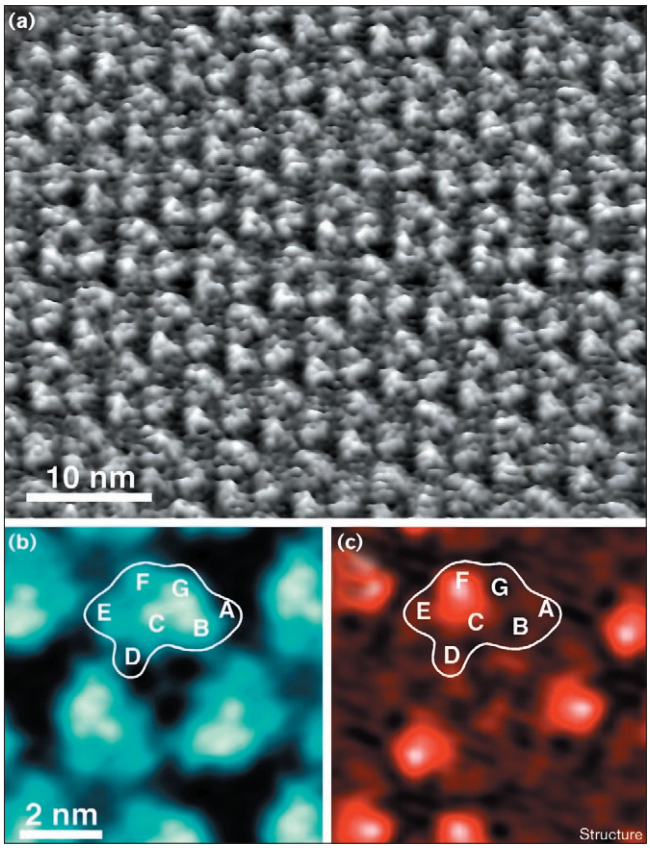

Cytoplasmic surface of the mutant IIIN PM digested with V8 protease. **(a)** AFM topograph recorded at low force (100 pN). **(b)** Threefold symmetrized correlation average of (a). **(c)** Standard deviation map of (b). The gray levels in the maps correspond to the height and standard deviation ranges shown in Table 1.

coordinate fluctuation, using the Gromacs package [30]. The results from this analysis were compared with the AFM occupancy measure for each structure. The first eigenvector describes a motion that is highly correlated with the AFM occupancy, and represents the change from a loop extending away from the surface, to a loop lying on the surface with the tip (the TTQ motif) over the C terminus. The major protrusion of the cytoplasmic surface of IIIN PM has an extension towards the C terminus that is not seen for the BR EF loop (compare Figure 2g with Figure 2i). The only type of conformation consistent with the AFM data is therefore concluded to be one where the tip of the loop lies close to, or over, the C terminus.

Several models were selected as representatives of particular types of conformations and subject to 100 picosecond molecular dynamics in water at 300K using the Gromacs package [30]. The first model was built by simply extending helices E and F (Figure 4b) as suggested from spin-labeling studies of the Rho EF loop in Rho itself [16]. The

Figure 4

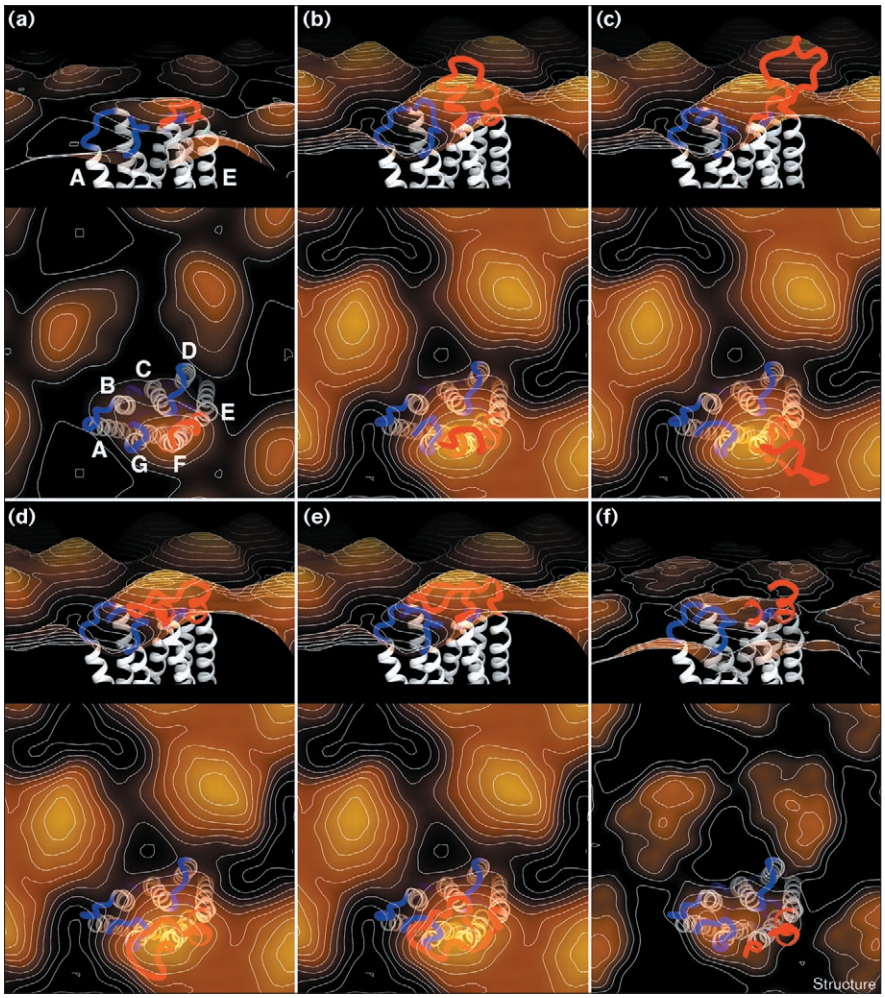

Comparison of AFM data of the cytoplasmic surfaces of PMs and atomic models of BR (A), the mutant IIIN, and the V8 protease digested mutant IIIN. **(a)** Wild-type BR (1QHJ retrieved from the PDB) superimposed on the cytoplasmic surface of the PM. The origin of the BR trimer model on the threefold axis was aligned with the center of the AFM envelope, producing a perfect fit (AFM occupancy = 1). **(b)** A mutant IIIN model with the helices E and F extended as far as possible into the Rho EF loops (AFM occupancy = 0.83). **(c)** A mutant IIIN model with one of many possible random loop conformations (AFM occupancy = 0.53). **(d)** A mutant IIIN model with the first part of the Rho EF loop lying over loop CD and the tip over the C terminus (AFM occupancy = 1). **(e)** A mutant IIIN model with the last part of the Rho EF loop lying over loop CD and the tip over the C terminus (AFM occupancy = 1). **(f)** The same model as in (d) but with the V8 protease digested segments omitted, superimposed on the corresponding digested surface of the PM. Bottom panels, view down the threefold axis; top panels, 65° rotated compared to the bottom panels. Transmembrane helices are shown in white, the EF loop in red, other loops in blue. Surfaces were contoured in 0.2 nm steps.

loop AFM occupancy is not very high, and the rigid helical framework is not consistent with the ease with which this loop can be displaced by the AFM tip (Figures 2k,l). Nevertheless, it remained in place during the molecular dynamics run, indicating that there are no serious steric problems with this conformation itself.

The Rho EF loop was next unraveled to form an extended coil with no regular structure (a typical conformation is shown in Figure 4c). Concoord sampling as well as molecular dynamics in water showed high flexibility, in agreement with the AFM data (Figure 2h). Most of these conformations, however, show low occupancies in the AFM envelope (down to 0.3). The chance that the Rho EF loop is really this unstructured and still gives a strong conformational signal during AFM imaging is considered remote.

Figure 4d shows a more probable conformation for the Rho EF loop, with the helices E and F only extending to the AFM surface up to the residues Gln237 and Glu249. The first part of the Rho EF loop lies over loop CD, and the tip follows the AFM contour over the C terminus. Conformations where these helical extensions are unraveled are also possible, but the general orientation of the loop towards the C terminus is clearly suggested by the AFM data.

An alternative loop conformation is one where the last part of the Rho EF loop lies over loop CD, with the tip again positioned over the C terminus (Figure 4e). The orientation switch from the previous conformation is comfortably accommodated in the AFM envelope, allowing the first part of the loop to pass outside the extension of helix F. Both these conformations are largely retained during molecular dynamics, with occupancies in the AFM envelope remaining close to one.

Figure 4f shows the conformation from Figure 4d with the V8 protease digested fragments removed, and superimposed onto the AFM topograph of the digested PM. The tops of helices E and F are clearly visible in the topograph,

emerging at residues Ala233 and Arg252. This agrees well with the cleavage after Glu249 at the top of helix F, corresponding to high flexibility in the standard deviation map. In contrast, the cleavage after Glu239 leaves a long loose end attached to helix E which is not apparent in the topograph (i.e., if such a segment can adopt a very large number of conformations, it is just averaged out during imaging). This illustrates the inability of the AFM to image segments that are really unstructured, further strengthening our interpretation that the intact Rho EF loop was well imaged.

Discussion

The cytoplasmic surface of Rho is an important interface where several proteins bind during the photoactivated signal cascade of vision. Determining the conformations and properties of the polypeptide loops involved in interactions with proteins such as transducin, rhodopsin kinase and arrestin, would provide information essential for understanding the dynamics of the process. Here we take a first step by studying one of the loop conformations grafted onto the known structure of BR.

AFM clearly shows the mutation of loop EF

The Rho EF loop was introduced into the place of the BR EF loop for two reasons: firstly, Rho and BR are both seven transmembrane α-helical proteins and their EF loops should be in similar locations; secondly, modifications of the BR EF loop did not show it to be structurally or functionally important [21,31,32]. The positions at which the Rho EF loop was inserted into BR are at the cytoplasmic ends of helices E and F (Figures 1a,b).

Comparing the E and F helices in several BR structures with those in a model of Rho based on medium-resolution electron crystallographic data [33], the ends of helices E and F are closer together in BR than in the Rho model (by ~ 2 Å). This is unlikely to perturb the structure of the Rho EF loop significantly. Furthermore, the angles at which the helices protrude from the membrane are similar.

It was shown that the modification of loop EF did not change the crystallographic lattice or the extracellular surface (Figure 2). This is not unexpected, because fragments of BR separated in the EF loop can be reconstituted with the chromophore [21,31,32]. The BR framework is thus not affected by the loop replacement, and provides a stable foundation for studying the Rho EF loop.

The major difference in the AFM images between the cytoplasmic surfaces of the IIIN and BR PMs is the much larger EF loop that projects towards the C terminus (Figure 2g). Even though the imaging was carried out at very low force, the possibility still exists that the AFM tip induced this loop conformation. Indeed, the time scales of image acquisition (several seconds) and dynamics of such a loop (pico- and nanoseconds) are separated by many orders of magnitude, so that the AFM tip is virtually stationary with respect to conformational changes. Nevertheless, it has been shown that the BR EF loop is well fitted into the major protrusion on the cytoplasmic side (especially in height) [20]. At salt concentrations of greater than 50 mM KCl, the Rho EF loop was poorly resolved, suggesting extensive deformation. At 50 mM KCl, the tip floats on an electrostatic cushion [24], avoiding deformation and allowing the Rho EF loop to assume an inherent conformation apparent in the AFM topographs. Furthermore, the Rho EF was imaged at a somewhat lower force to generate the same quality images as for BR (Table 1). Thus we are confident that the loop conformation revealed by AFM is a highly probable one.

Because the difference in the cytoplasmic surfaces of BR and IIIN also includes a region above the C terminus, the question arises as to the influence of the long C terminus (~20 residues) on the conformation of the Rho EF loop. AFM topographs of the cytoplasmic surface BR, IIIN, and digested IIIN did not reveal any indication of the C terminus, and the simplest interpretation is that it is too unstructured to allow imaging. Consequently, we assume that it also does not affect the conformation of the Rho EF loop on the BR framework.

The flexibility and helicity of the Rho EF loop

The AFM data show a particular conformation for the Rho EF loop grafted onto the BR framework, but also indicates that this loop is rather flexible. The Rho EF loop can be displaced by lower forces than the BR EF loop, and at high force, it shows even more displacement than the BR EF loop (Figures 2g,h). The height difference between the low-force and high-force images indicate that the energy to displace the Rho EF loop is 7–13 kcal/mol, somewhat higher than the ~ 4 kcal/mol required for the BR EF loop. This difference could be attributed to the larger size of the Rho EF loop. It is therefore unlikely that the Rho EF loop has a more rigid structure than the BR EF loop.

The stability of the Rho EF loop has a direct implication for its structure. If helices E and F were extended as far as possible into Rho EF (as in Figure 4b), it would form a more rigid structure extending at least 2 nm above the lipid bilayer surface. This is clearly inconsistent with either the AFM height data (maximum height = 1.5 nm) and the flexibility of the loop. In addition, such a model is inconsistent with the peak in the standard deviation map over loop CD (Figure 2h). The Rho EF loop inserted into BR might therefore be only partially helical in nature.

The AFM data limit the extension of the helices E and F into the Rho EF loop to about residues Gln237 and Glu249, respectively (all residue numbers given are for the Rho EF loop in Rho). The E and F helices in BR continue

to about Glu161 and Phe165 (Glu232 and Arg252 in the Rho EF loop, respectively), indicating at most only one additional helical turn in each helix that extends into the Rho EF loop.

Probable conformations of the Rho EF loop

In the AFM topograph of IIIN PM, the Rho EF loop clearly points towards the C terminus (Figures 2g, 4d, 4e). Two types of loop conformation can be fitted into this envelope. The first model (Figure 4d), starts with the extension of helix E, proceeds close to loop CD, the tip suspended above the C terminus, and finally ends in a small extension of helix F. This loop can be inverted (Figure 4e), so that the first part of the loop passes over helix F, the tip crosses over the C terminus, and the last part lies close to the CD loop. Both conformations show high AFM occupancy during molecular dynamics runs, which suggests that they are equally good candidates for the conformation of Rho EF.

The relevance of these conformations can only be judged by agreement with other studies and the location of key residues in the Rho EF loop. The extension of helix E into the Rho EF loop up to Gln237 (Rho numbering) is now supported by our AFM data, systematic cysteine substitution coupled with transducin activation [11], and spin-labeling of these cysteine mutants [16].

The extension of the F helix is less clear. On the basis of the results of spin-labeling studies it was suggested that helix F is extended as far as Ser240 [16]. However, the interaction with transducin was inhibited in the oxidized cysteine double mutants for the whole segment from Glu247 to Thr251 [34], a region also implicated by mutagenesis studies [12]. This is inconsistent with an α-helical conformation and the limits imposed by our AFM data. The conformation shown in Figure 4d, in which the F helix starts around Arg252, features a flexible stretch from Glu247 to Thr251 that would allow access to loop CD. The conformation in Figure 4e is even more favourable, because the Glu247–Thr251 stretch passes very close to the CD loop (also see Figure 5).

Figure 5

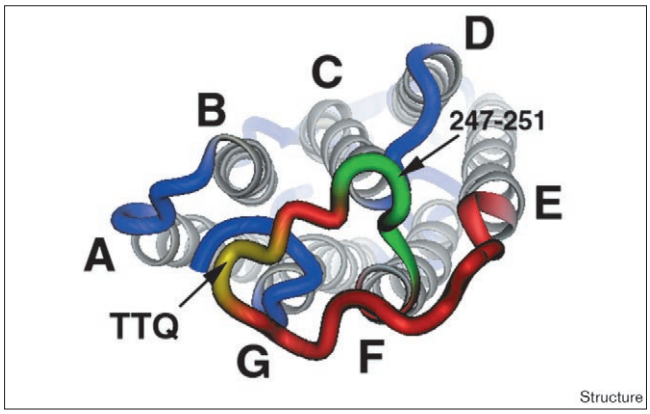

Relevance of a probable conformation of the third cytoplasmic loop of Rho grafted onto BR. A model of the IIIN mutant is shown from the cytoplasmic side with the transmembrane helices in gray and the loops AB and CD, and the C terminus in blue. The EF loop is colored red with yellow indicating the TTQ motif involved in transducin binding and green indicating a region shown to cross-link to loop CD in double-cysteine mutants.

The tripeptide Thr242–Thr243–Gln244 at the tip of the EF loop is a key motif for transducin binding, as shown with loop deletions and amino acid substitutions [10], and a series of cysteine mutants [11]. In the two probable conformations (Figures 4d,e), this motif is located in about the same place above the center of helices A, B, C and G (Figure 5). It is therefore easily accessible and close to the CD loop, consistent with the binding of transducin to these loops in Rho.

Rhodopsin kinase binding to light-activated Rho involves a sequence-specific interaction with the CD loop, whereas the EF loop only needs to be there and structured [13,14]. When the EF loop is cut with V8 protease, phosphorylation by rhodopsin kinase drops to 50%. Here we showed that a segment of the Rho EF loop in the IIIN mutant is excised by V8 protease, and that the remaining parts of the loop become unstructured.

The binding of arrestin to phosphorylated, light-activated Rho involves the AB loop weakly, and the EF loop strongly [15]. Arrestin competes with transducin, and might require the same motif as transducin. This is suggested by a peptide competition study, in which the intact EF loop peptide competed much more effectively with arrestin than with either of two peptides corresponding to the EF loop cleaved in the TTQ motif [35]. This motif is located very close to the AB loop in both probable conformations of the Rho EF loop in IIIN (Figures 4d,e).

In our study we took the first step in converting the BR cytoplasmic surface to that of Rho, by transferring the most prominent loop, the third or EF loop. The biological activity of the IIIN mutant is difficult to assess at this stage, because all three proteins interacting with the EF loop on Rho, that is transducin, rhodopsin kinase and arrestin, require at least one other Rho loop as well. Thus, our mutant will almost certainly be incapable of binding one of these proteins. It is also possible that the Rho EF loop will adopt a different conformation in the presence of the other cytoplasmic loops of Rho. Here we present the techniques and a first example, which will form the basis for future studies to unravel the complicated interactions at the cytoplasmic surface of Rho. Such experiments will focus on the flexibility and conformational variability of the Rho loops on their native framework, as well as spliced onto the BR framework. Knowledge of the effects of

studying such loops in different contexts will allow the extension of this approach to study the surfaces and loops of other G-protein-coupled receptors.

Biological implications

On light activation, the rhodopsin (Rho) cytoplasmic surface interacts with several proteins to initiate and control the visual signal. Understanding these interactions requires knowledge of the structures of the loops constituting the cytoplasmic surface, but little such information is available. One such loop, the third cytoplasmic or EF loop (Rho EF), was used to replace the corresponding loop in bacteriorhodopsin (BR), a closely related protein from *Halobacterium salinarum* with a known atomic structure. Atomic force microscopy (AFM) was used to assess the changes introduced in the mutant BR (called IIIN). The major difference is a larger protrusion with a new shape on the cytoplasmic side, associated with the longer EF loop. This was confirmed by digestion with V8 protease, which excised ten residues from the Rho EF loop in IIIN, and also removed the large protrusion on the cytoplasmic surface of IIIN.

The Rho EF loop shows high flexibility on the BR framework as measured by AFM, consistent with the large number of allowed conformations generated by modeling the loop. However, only a small fraction of the allowed conformations is consistent with the envelope derived from AFM data, suggesting that the loop does adopt a loosely defined conformation.

The most likely conformations of the Rho EF loop involve some extension of helices E and F, with the tip of the loop situated over the C terminus and part of it passing close by the CD loop. The TTQ motif (in single-letter amino acid code), which is important for binding to transducin and possibly arrestin, is positioned close to the AB and CD loops, which are also required for interaction with arrestin and transducin in Rho. The C-terminal part of the Rho EF loop is probably located close to the CD loop, whereas the N-terminal part passes over or outside helix F. This provides information about the possible conformations of the Rho EF loop grafted onto the BR framework, and suggests the likely conformations within Rho itself, thus providing a new view of its structure.

Materials and methods

Replacement of the BR EF loop with the Rho loop III

The vector pTZOPbopcisIII contains a construct derived from the *bop* gene coding for bacterio-opsin [36] modified by replacing 27 bp coding for the EF loop (eight residues) with 75 bp from the *bRho* gene coding for the bovine Rho third cytoplasmic loop (24 residues) (Figure 1). Because pTZOPbopcisIII is an *Escherichia coli* plasmid, it could not be used for expression in *H. salinarum*. Therefore, the *Nhe*I-*Not*I fragment of the *bop* gene carrying the elongated EF loop was recloned into the *H. salinarum–E. coli* shuttle vector pUS-Mev [8,37]. The resulting vector was denominated pHXIII (Halo Xpression of BR with III loop from Rho). For reasons not relevant here, Asp96 was mutated to asparagine by overlap extension and the polymerase chain reaction (PCR) product was cloned into the shuttle vector pUS-Mev. The resulting plasmid was denominated pHXIIIN (Halo Xpression of BR with III loop from Rho and point mutation Asp96Asn). For confirmation of the *H. salinarum* transformants total DNA was isolated, the bacterio-opsin gene amplified by PCR and sequenced.

Expression and preparation of PM

pHXIIIN was introduced into the *H. salinarum* strain SNOB, which is a bacterio-opsin gene-deficient derivative of the strain S9 (S9 without bop) [8]. Mutant purple membrane (IIIN PM) was isolated from this strain, and wild-type PM was isolated from strain ET 1001 [38]. The membranes were frozen and stored in buffer at –70°C.

SDS–PAGE

Aliquots of wild-type, and mutated BR were subjected to SDS–PAGE. SDS concentrations of the stacking gel and of the separating gel were 4% and 15%, respectively.

V8 protease treatment of PM

The wild-type and mutant PM was digested with V8 protease (endoproteinase Glu-C; Boehringer Mannheim, Germany). A digestion solution with 0.5 mg PM in 100 µl Tris-HCl pH 7.9 and 1 µg protease in 10 µl deionized water was incubated for 18 h at 25°C. Digestion samples were then pelleted and washed three times in deionized water at 150.000 × g for 3 min. An aliquot of digested PM was checked using SDS–PAGE to assess the completeness of digestion (Figure 1c).

Electrospray ionization mass spectrometry

Mass spectrometry was done according to Hufnagel *et al.* [39].

Atomic force microscopy

All buffers for AFM imaging were made with ultrapure water (≈18 MΩ/cm) to avoid contamination. Chemicals were p.a. grade and purchased from SIGMA Chemie AG (Buchs, Switzerland). To minimize contamination of surfaces during exposure to ambient air, sample supports were prepared immediately before use. The samples were checked by conventional negative stain electron microscopy [40] and by SDS–PAGE before use.

The PM was diluted to a concentration of 10 µg/ml in 300 mM KCl, pH 7.8, 10 mM Tris-HCl prior to adsorption to freshly cleaved mica [41]. After an adsorption time of 20 min the sample was gently washed with the imaging buffer (10 mM Tris-HCl, pH 7.8, 100–150 mM KCl) to remove membranes that were not firmly attached to the support. The specimen was mounted on the piezoelectric scanner of the atomic force microscope (Nanoscope III, Digital Instruments, Santa Barbara, USA) which was equipped with a liquid cell. The spring of the fluid cell was modified with an extra strong spring to hold the cantilever more tightly. Cantilevers used had nominal force constants of k = 0.09 N/m or k = 0.02 N/m and oxide sharpened Si_3N_4 tips (Olympus Ltd., Tokyo, Japan). After thermal relaxation for 15–30 min, the drift of the cantilever deflection angle was at a minimum. Initial engagement of the tip was then performed by setting the scan size zero to minimize specimen deformation or tip contamination. Prior to scanning the sample, the operating point of the microscope was set to forces below 0.5 nN. All measurements were performed under ambient pressure and at room temperature (21°C).

At low magnification (frame size approximately 600 nm) images were recorded in the error signal mode acquiring the deflection and height signals simultaneously. The deflection signal was minimized by optimizing gains and scan speed. The scan speed was roughly linear to the scan size, 4–8 lines per second for lower magnifications (frame size 13–0.5 µm, respectively) and 10–17 lines per second for higher magnifications (frame sizes 130–80 nm, respectively). At high magnification, the deformation of the sample [42] was minimized by comparing the height profiles acquired in trace and retrace direction, and at different

scan angles. The applied force was corrected manually to compensate for the thermal drift of the microscope.

The 'E' and 'J'– piezoelectric scanners used had a scan range of $12 \times 12\ \mu m^2$ and of $100 \times 100\ \mu m^2$, respectively. Calibration of the scanner was carried out using transition metal dichalcogenides [43] as substrate references. The lateral calibration was carried out by comparing the lattice constants of the layered surface, and for calibration in z-direction, defects (large holes or steps) were used [41].

High-resolution AFM imaging

The distance-dependent electrostatic double-layer (EDL) interaction between AFM tip and purple membrane was adjusted to a repulsive maximum of about 0.1 nN and an interaction length between 2 and 5 nm via the selection of pH and electrolyte concentration of the buffer solution. The electrostatic double layer interaction damps the AFM tip by distributing the applied force (≈ 0.1 nN) over a relatively large sample area. The AFM tip then floats on a cushion of electrostatic repulsion, while a small microscopic protrusion contours the biological surface at a significantly minimized interaction force and interaction area. Consequently, the deformation of the native proteins was minimized enhancing the lateral resolution to about 6 Å [22].

Image processing

For image processing, the raw data (size 512×512 pixel) of topographs acquired in the trace and retrace directions were transferred to a Digital Equipment ALPHA workstation and analyzed using the SEMPER image processing system [44]. For correlation averaging, a well-preserved unit cell was selected from the raw data and cross-correlated with the topograph [45]. Unit cells were then extracted according to the peak coordinates and averaged. The resulting correlation average was used as reference for refinement cycles [46]. Correlation averaged unit cells were finally threefold symmetrized. To assess the standard deviation individual unit cells were extracted according to the coordinates of their correlation peaks and were aligned rotationally as well as translationally before single particle averaging [47]. The standard deviation from the averaged topograph was then calculated [48]. Resolution was assessed using Fourier ring correlation (FRC) [45] and the spectral signal-to-noise ratio (SSNR) [49].

Constructing an AFM envelope map

AFM topographs were converted to 3D objects so that the 'inside' has unit density and the 'outside' has zero density, using the transition function for the density at each point (x,y,z) [50]:

$$\rho(x,y,z) = \frac{1}{1 + e^{a((z-h(x,y))/\sigma)}} \qquad (1)$$

where h(x,y) is the height value associated with each gray value in the AFM topograph, σ is a width value similar to a Gaussian width parameter (i.e., the 'softness' or transition gradient at the surface) taken from the AFM standard deviation maps, and $a = 1.618$ is an empirical constant. The 3D surfaces of the extracellular and cytoplasmic topographs were calculated and combined to give an envelope with a minimum separation between the surfaces of 4.4 nm (i.e., the width of the lipid bilayer as determined by AFM). The position of the envelope was adjusted to fit the BR model, further used for visualization and calculating AFM occupancy (see below). All image manipulations were done with programs bsurf, bimg and bop, from the Bsoft package (http://www.mih.unibas.ch/Homepages/heymann/Bsoft.html).

Modeling the Rho EF loop

As in the experimental construction of the IIIN mutant (see above), eight residues of the BR EF loop from the model 1qhj.pdb [26] retrieved from the PDB were replaced by 24 residues from the Rho EF loop using the program WHAT IF [27]. Many different loop conformations were generated manually in the program O [28], and automatically using the package Concoord [29]. The stability of some loop conformations was checked by molecular dynamics simulation in water using Gromacs package, version 2.0 [30]. The agreement between loop conformations and the AFM 3D envelope of IIIN was assessed by scoring the number of loop atoms falling within the envelope.

AFM occupancy

The BR framework (i.e., excluding the EF loop) of each new model was fitted to the original BR model, using the program LSQMAN [51]. The model was then converted to a real space density using a Gaussian sphere for each atom at a resolution of 5 Å (method described in [50]). The occupancy for each atom within the AFM envelope is defined as:

$$q = \begin{cases} 1 & \text{if } \rho_{AFM} > \rho_{MODEL} \\ \dfrac{\rho_{AFM}}{\rho_{MODEL}} & \text{otherwise} \end{cases} \qquad (2)$$

if $\rho_{AFM} > \rho_{MODEL}$ otherwise where ρ_{AFM} and ρ_{MODEL} are the densities at the atomic coordinates for the AFM envelope and the model, respectively. The two densities were scaled to have the same minimum and maximum before calculating the AFM occupancy. The density and AFM occupancy calculations were done using the program bgex in the Bsoft package.

Acknowledgements

We thank N Dencher for critical reading of the manuscript and A Philippsen for discussions and helpful assistance in using his program Dino for visualization (http://www.biozentrum.unibas.ch/~xray/dino). This work was supported by the Maurice E Müller Foundation, the Swiss National Foundation for Scientific Research (NFP grant 31-424335.94 to AE) and the European Union (grant EC BIO4-CT960472 to AE), and the Sonderforschungsbereich (SFB533 granted to MP and DO).

References

1. Krebs, A., Villa, C., Edwards, P.C. & Schertler, G.F. (1998). Characterisation of an improved two-dimensional p22121 crystal from bovine rhodopsin. *J. Mol. Biol.* **282**, 991-1003.
2. Unger, V.M., Hargrave, P.A., Baldwin, J.M. & Schertler, G.F. (1997). Arrangement of rhodopsin transmembrane α helices. *Nature* **389**, 203-206.
3. Dencher, N.A., Dresselhaus, D., Zaccai, G. & Büldt, G. (1989). Structural changes in bacteriorhodopsin during proton translocation revealed by neutron diffraction. *Proc. Natl Acad. Sci. USA* **86**, 7876-7879.
4. Subramaniam, S., Gerstein, M., Oesterhelt, D. & Henderson, R. (1993). Electron diffraction analysis of structural changes in the photocycle of bacteriorhodopsin. *EMBO J.* **12**, 1-8.
5. Steinhoff, H.-J., Mollaaghababa, R., Altenbach, C., Khorana, H.G. & Hubbell, W.L. (1995). Site-directed spin-labeling studies of structure and dynamics in bacteriorhodopsin. *Biophys. Chem.* **56**, 89-94.
6. Steinhoff, H.-J., Mollaaghababa, R., Altenbach, C., Hideg, K., Khorana, H.G. & Hubbell, W.L. (1994). Time-resolved detection of structural changes during the photocycle of spin-labeled bacteriorhodopsin. *Science* **266**, 105-107.
7. Essen, L., Siegert, R., Lehmann, W.D. & Oesterhelt, D. (1998). Lipid patches in membrane protein oligomers: crystal structure of the bacteriorhodopsin–lipid complex. *Proc. Natl Acad. Sci. USA* **95**, 11673-11678.
8. Pfeiffer, M., Rink, T., Gerwert, K., Oesterhelt, D. & Steinhoff, H.-J. (1999). Site-directed spin-labeling reveals the orientation of the amino acid sidechains in the E–F loop of bacteriorhodopsin. *J. Mol. Biol.* **287**, 163-171.
9. Steinhoff, H.-J., Müller, M., Beier, C. & Pfeiffer, M. (2000). Molecular dynamics simulation and EPR spectroscopy of nitroxide sidechains in bacteriorhodopsin. *J. Mol. Liquids* **84**, 17-27.
10. Franke, R.R., Sakmar, T.P., Graham, R.M. & Khorana, H.G. (1992). Structure and function in rhodopsin. Studies of the interaction between the rhodopsin cytoplasmic domain and transducin. *J. Biol. Chem.* **267**, 14767-14774.
11. Yang, K., Farrens, D.L., Hubbell, W.L. & Khorana, H.G. (1996). Structure and function in rhodopsin. Single cysteine substitution mutants in the cytoplasmic interhelical E–F loop region show position-specific effects in transducin activation. *Biochemistry* **35**, 12464-12469.

12. Acharya, S., Saad, Y. & Karnik, S.S. (1997). Transducin-α C-terminal peptide binding site consists of C–D and E–F loops of rhodopsin. *J. Biol. Chem.* **272**, 6519-6524.
13. Palczewski, K., Buczylko, J., Kaplan, M.W., Polans, A.S. & Crabb, J.W. (1991). Mechanism of rhodopsin kinase activation. *J. Biol. Chem.* **266**, 12949-12955.
14. Thurmond, R.L., Creuzenet, C., Reeves, P.J. & Khorana, H.G. (1997). Structure and function in rhodopsin: peptide sequences in the cytoplasmic loops of rhodopsin are intimately involved in interaction with rhodopsin kinase. *Proc. Natl Acad. Sci. USA* **94**, 1715-1720.
15. Krupnick, J.G., Gurevich, V.V., Schepers, T., Hamm, H.E. & Benovic, J.L. (1994). Arrestin–rhodopsin interaction. Multi-site binding delineated by peptide inhibition. *J. Biol. Chem.* **269**, 3226-3232.
16. Altenbach, C., Yang, K., Farrens, D.L., Farahbakhsh, Z.T., Khorana, H.G. & Hubbell, W.L. (1996). Structural features and light-dependent changes in the cytoplasmic interhelical E–F loop region of rhodopsin: a site-directed spin-labeling study. *Biochemistry* **35**, 12470-12478.
17. Yeagle, P.L., Alderfer, J.L. & Albert, A.D. (1997). Three-dimensional structure of the cytoplasmic face of the G protein receptor rhodopsin. *Biochemistry* **36**, 9649-9654.
18. Shao, Z.F. & Yang, J. (1995). Progress in high resolution atomic force microscopy in biology. *Quart. Rev. Biophys.* **28**, 195-251.
19. Engel, A., Schoenenberger, C.-A. & Müller, D.J. (1997). High resolution imaging of native biological sample surfaces using scanning probe microscopy. *Curr. Opin. Struct. Biol.* **7**, 279-284.
20. Heymann, J.B., *et al.*, & Engel, A. (1999). Charting the surfaces of the purple membrane. *J. Struct. Biol.* **128**, 243-249.
21. Sigrist, H., Wenger, R.H., Kislig, E. & Wüthrich, M. (1988). Refolding of bacteriorhodopsin. Protease V8 fragmentation and chromophore reconstitution from proteolytic V8 fragments. *Eur. J. Biochem.* **177**, 125-133.
22. Müller, D.J., Sass, H.-J., Müller, S., Büldt, G. & Engel, A. (1999). Surface structures of native bacteriorhodopsin depend on the molecular packing arrangement in the membrane. *J. Mol. Biol.* **285**, 1903-1909.
23. Müller, D.J., Schoenenberger, C.-A., Büldt, G. & Engel, A. (1996). Immuno-atomic force microscopy of purple membrane. *Biophys. J.* **70**, 1796-1802.
24. Müller, D.J., Fotiadis, D., Scheuring, S., Müller, S.A. & Engel, A. (1999). Electrostatically balanced subnanometer imaging of biological specimens by atomic force microscopy. *Biophys. J.* **76**, 1101-1111.
25. Müller, D.J., Büldt, G. & Engel, A. (1995). Force-induced conformational change of bacteriorhodopsin. *J. Mol. Biol.* **249**, 239-243.
26. Belrhali, H., *et al.*, & Pebay-Peyroula, E. (1999). Protein, lipid and water organization in bacteriorhodopsin: a molecular view of the purple membrane at 1.9 Å resolution. *Structure* **7**, 909-917.
27. Vriend, G. (1990). WHAT IF: A molecular modeling and drug design program. *J. Mol. Graph.* **8**, 52-56.
28. Jones, T.A. & Kjeldgaard, M. (1998). *O – The Manual (version 6.2)*. University of Uppsala.
29. de Groot, B.L., van Aalten, D.M.F., Scheek, R.M., Amadei, A., Vriend, G. & Berendsen, H.J.C. (1997). Prediction of protein conformational freedom from distance constraints. *Proteins* **29**, 240-251.
30. van der Spoel, D., *et al.*, & Berendsen, H.J.C. (1999). *Gromacs User Manual. Version 2.0.* eds), pp 223, University of Groningen, Groningen, The Netherlands.
31. Liao, M.-J., Huang, K.-S. & Khorana, H.G. (1984). Regeneration of native bacteriorhodopsin structure from fragments. *J. Biol. Chem.* **259**, 4200-4204.
32. Kataoka, M., Kahn, T.W., Tsujiuchi, Y., Engelman, D.M. & Tokunaga, F. (1992). Bacteriorhodopsin reconstituted from two individual helices and the complementary five-helix fragment is photoactive. *Photochem. Photobiol.* **56**, 895-901.
33. Baldwin, J.M., Schertler, G.F. & Unger, V.M. (1997). An α-carbon template for the transmembrane helices in the rhodopsin family of G-protein-coupled receptors. *J. Mol. Biol.* **272**, 144-164.
34. Farrens, D.L., Altenbach, C., Yang, K., Hubbell, W.L. & Khorana, H.G. (1996). Requirement of rigid-body motion of transmembrane helices for light activation of rhodopsin. *Science* **274**, 768-770.
35. Krupnick, J.G., Gurevich, V.V. & Benovic, J.L. (1997). Mechanism of quenching of phototransduction. Binding competition between arrestin and transducin for phosphorhodopsin. *J. Biol. Chem.* **272**, 18125-18131.
36. Hildebrandt, V., *et al.*, & Büldt, G. (1989). Genetic transfer of the pigment bacteriorhodopsin into the eukaryote *Schizosaccharomyces pombe*. *FEBS Let.* **243**, 137-140.
37. Schweiger, U. (1996). *Funktionelle Charakterisierung der Retinalbindungstasche von Bakteriorhodopsin durch spezifische Mutagenese*. PhD thesis, Leopold-Franzens-Universität, Innsbruck, Austria.
38. Oesterhelt, D. & Stoeckenius, W. (1974). Isolation of the cell membrane of *Halobacterium halobium* and its fraction into red and purple membrane. *Meth. Enzymol.* **31**, 667-678.
39. Hufnagel, P., Schweiger, U., Eckerskorn, C. & Oesterhelt, D. (1996). Electrospray ionization mass spectrometry of genetically and chemically modified bacteriorhodopsins. *Anal. Biochem.* **243**, 46-54.
40. Bremer, A., Henn, C., Engel, A., Baumeister, W. & Aebi, U. (1992). Has negative stain still a place in biomacromolecular electron microscopy? *Ultramicr.* **46**, 85-111.
41. Müller, D.J. & Engel, A. (1997). The height of biomolecules measured with the atomic force microscope depends on electrostatic interactions. *Biophys. J.* **73**, 1633-1644.
42. Weisenhorn, A.L., Khorsandi, M., Kasas, S., Gotzos, V. & Butt, H.-J. (1993). Deformation and height anomaly of soft surfaces studied with an AFM. *Nanotechnol.* **4**, 106-113.
43. Wilson, J.A. & Yoffe, A.D. (1969). The transition metal dichalcogenides discussion and interpretation of the observed optical, electrical and structural properties. *Advanc. Phys.* **18**, 193-335.
44. Saxton, W.O., Pitt, T.J. & Horner, M. (1979). Digital image processing: the semper system. *Ultramicr.* **4**, 343-354.
45. Saxton, W.O. & Baumeister, W. (1982). The correlation averaging of a regularly arranged bacterial cell envelope protein. *J. Microsc.* **127**, 127-138.
46. Saxton, W.O., Baumeister, W. & Hahn, M. (1984). Three-dimensional reconstruction of imperfect two-dimensional crystals. *Ultramicr.* **13**, 57-70.
47. Frank, J., Bretaudiere, J.-P., Carazo, J.-M., Veschoor, A. & Wagenknecht, T. (1987). Classification of images of biomolecular assemblies: a study of ribosomes and ribosomal subunits of *Escherichia coli*. *J. Microsc.* **150**, 99-115.
48. Schabert, F.A. & Engel, A. (1994). Reproducible acquisition of *Escherichia coli* porin surface topographs by atomic force microscopy. *Biophys. J.* **67**, 2394-2403.
49. Unser, M., Trus, B.L. & Steven, A.C. (1987). A new resolution criterion based on spectral signal-to-noise ratios. *Ultramicr.* **23**, 39-52.
50. Pittet, J.-J., Henn, C., Engel, A. & Heymann, J.B. (1999). Visualizing 3D data obtained from microscopy on the Internet. *J. Struct. Biol.* **125**, 123-132.
51. Kleywegt, G.J. (1996). Use of noncrystallographic symmetry in protein structure refinement. *Acta Crystallogr. D* **52**, 842-857.

Because *Structure with Folding & Design* operates a 'Continuous Publication System' for Research Papers, this paper has been published on the internet before being printed (accessed from http://biomednet.com/cbiology/str). For further information, see the explanation on the contents page.